

Structural and Electrical Characterization of Bi_2Se_3 Nanostructures Grown by Metalorganic Chemical Vapor Deposition

L. D. Alegria,[†] M. D. Schroer,[†] A. Chatterjee,[†] G. R. Poirier,[‡] M. Pretko,[†]
S. K. Patel,[†] and J. R. Petta^{*,†}

*Department of Physics, Princeton University, Princeton, New Jersey 08544, and Princeton
Institute for the Science and Technology of Materials, Princeton University, Princeton, New
Jersey 08544*

E-mail: petta@princeton.edu

Abstract

We characterize nanostructures of Bi_2Se_3 that are grown via metalorganic chemical vapor deposition using the precursors diethyl selenium and trimethyl bismuth. By adjusting growth parameters, we obtain either single-crystalline ribbons up to $10\ \mu\text{m}$ long or thin micron-sized platelets. Four-terminal resistance measurements yield a sample resistivity of $4\ \text{m}\Omega\text{-cm}$. We observe weak anti-localization and extract a phase coherence length $l_\phi = 178\ \text{nm}$ and spin-orbit length $l_{\text{so}} = 93\ \text{nm}$ at $T = 0.29\ \text{K}$. Our results are consistent with previous measurements on exfoliated samples and samples grown via physical vapor deposition.

Keywords: Bi_2Se_3 , nanoribbon, MOCVD, VLS, topological insulator

*To whom correspondence should be addressed

[†]Department of Physics, Princeton University, Princeton, New Jersey 08544

[‡]Princeton Institute for the Science and Technology of Materials, Princeton University, Princeton, New Jersey 08544

Bi_2Se_3 is a strong topological insulator (TI) with a single Dirac cone and chiral spin texture.^{1,2} Surface-sensitive probes have directly accessed the topological surface states, but transport measurements have proven difficult due to bulk contributions to the conductivity.^{3,4} Efforts to isolate surface transport properties include mechanical exfoliation, electrical gating, and chemical doping.⁵⁻¹⁰ Another way to reduce bulk conduction is to directly synthesize nanostructures with a large surface-to-volume ratio.¹¹⁻¹³ We demonstrate the controlled synthesis of Bi_2Se_3 nanoribbons using metal-organic chemical vapor deposition (MOCVD), a standard process for rational nanostructure synthesis, and we characterize the nanoribbons using electron microscopy and low-temperature magnetotransport measurements.

Bi_2Se_3 has been the focus of many TI experiments due to its comparatively large bulk band gap of 0.35 eV and simple surface band structure.³ Bi_2Se_3 adopts a rhombohedral structure belonging to the space group $D_{3d}^5 (R\bar{3}m)$.¹⁴ The crystal consists of 2D hexagonal lattices of either Se or Bi, which stack according to the sequence Se-Bi-Se-Bi-Se. Adjacent layers of Se are Van der Waals bonded, such that Bi_2Se_3 preferentially forms sheet-like structures. In addition to TI research, Bi_2Se_3 and related compounds are of interest for high performance thermoelectric materials.¹⁵ In that context, various nanostructures, including quintuple layer nanotubes, have been synthesized by co-reduction from solution, template-assisted electrodeposition, and solid-source vapor transport.¹⁶⁻¹⁸ Many of these convenient methods have subsequently been employed for TI experiments.^{11,19} However, factors including sample purity, uniformity of growth, and precise control over the Se/Bi flux ratio favor molecular beam epitaxy (MBE) and MOCVD.

Previous MOCVD studies of Bi_2Se_3 have focused on the development of appropriate precursors and growth conditions for thin film growth.²⁰ In one case the formation of Bi_2Se_3 platelets alongside BiPO_4 nanowires was observed in the decomposition of the oxygen and phosphorus-containing bismuth complex $\text{Bi}[\text{Se}_2\text{P}(\text{O}i\text{Pr})_2]_3$.²¹ Here we pursue the MOCVD synthesis of Bi_2Se_3 nanostructures using separate Se and Bi precursors, allowing individual control of the precursor partial pressures.

We grow nanostructures in a laboratory-scale MOCVD reactor, similar to one used to produce

high quality InAs nanowires.^{22,23} Mass flow controllers admit fixed flows of H₂ carrier gas through two bubblers containing the liquid metal-organic precursors trimethyl bismuth (TMBi) and diethyl selenium (DESe).²⁴ The precursor vapors and H₂ gas flow into a cold-walled chamber and impinge on a heated sample holder containing a Si (100) substrate that is prepared with a 5 nm thick Au seed layer.

A uniform layer of Bi₂Se₃ nanostructures forms on the ~ 1 cm² substrate under a range of growth conditions. We generally obtain two different types of structures: nanoribbons with 10 – 30 nm thickness and lengths of several microns, or nanoplates as thin as 10 nm with roughly 1 μ m lateral dimensions. The growth temperature, T_g , and precursor partial pressure ratio, $r = p_{\text{DESe}}/p_{\text{TMBi}}$, determine which type of structures we obtain. Figure 1 shows scanning electron microscope (SEM) images of samples obtained for a range of growth parameters. High-yield growth occurs for $T_g = 470$ °C, with a chamber pressure $P = 100$ Torr, carrier gas flow of 600 sccm H₂, TMBi partial pressure $p_{\text{TMBi}} = 1 \times 10^{-5}$ atm, and $r = 30$. Typical growth times are 15 minutes. In order to systematically study changes in the growth morphology with reaction conditions, we take this parameter set as a reference from which we vary individual parameters. Under these conditions, nanoribbon growth begins once r exceeds ~ 7 . Between $r = 7 - 33$, the reaction products transition from narrow ribbons to wide ribbons and plates, accompanied by an increase in density. Little change in morphology is observed above $r = 33$ which suggests that Bi limits the growth at such high precursor ratios.

We also consider the temperature and time dependence of the growth. With all other growth parameters fixed as above, nanoribbons are obtained at a growth temperature $T_g = 470$ °C and widen into plates above 480 °C (see Figure 1d). Longer growth runs of 30 minutes produced ribbons up to 10 μ m long, maintaining cross sections on the order of 10×100 nm².

In general, epitaxial nanostructure growth can occur by several mechanisms, including vapor-liquid-solid (VLS) and vapor-solid (VS) growth.^{25,26} In typical VLS growth, a metal droplet nucleates crystal growth and determines the nanowire diameter. Bi₂Se₃ nanostructure growth has been demonstrated with and without seed particle involvement.^{19,27} Under the above growth conditions,

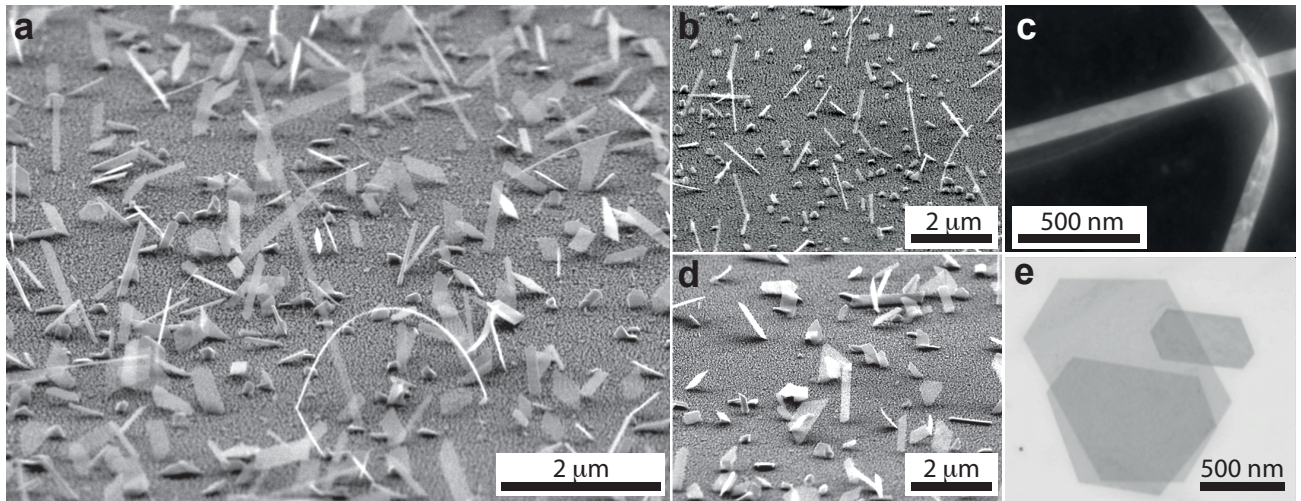


Figure 1: Bi₂Se₃ nanoribbons and platelets: (a,b,d) SEM images of as-grown samples, and (c,e) images obtained after deposition on TEM grids. (a) Diverse growth is obtained from a 15 minute growth run on a Si (100) substrate with 5 nm Au seed layer, with $T_g = 470$ °C, $P = 100$ Torr, 600 sccm H₂ carrier gas flow, TMBi partial pressure $p_{\text{TMBi}} = 1 \times 10^{-5}$ atm, and precursor ratio $r = 33$. (b) A reduced precursor ratio $r = 12$ results in narrow nanoribbons of comparatively well-defined widths 70 ± 20 nm. (c) Dark field scanning transmission electron microscope (STEM) image of two nanoribbons with 85×10 nm² cross section. The nanoribbons are single crystal and show stress induced fringes. (d) We obtain platelets at $r = 30$ and an elevated growth temperature $T_g = 490$ °C. (e) ~ 1 μm² platelets imaged by STEM.

we find that growth occurs when the Si substrate is prepared with a 5 nm film of Au, but not on bare Si. We do not observe a gold particle at the free end of the nanoribbon, as seen in the solid-source growth method described by Kong et al.¹⁹ Instead, many ribbons clearly originate from gold nanoparticles on the substrate. VLS growth in our MOCVD growth process may therefore be occurring at the base of the nanowire via root catalyzed growth, as has been observed in other materials.²⁵

We establish that the samples are single-crystalline Bi_2Se_3 using transmission electron microscopy (TEM). The nanostructures are first freed from the growth substrate by sonication in ethanol and then transferred to porous carbon TEM grids for imaging in a Phillips CM200 transmission electron microscope. Figure 2 displays a high resolution TEM analysis of a typical nanoribbon. By performing selected-area electron diffraction at various points along the nanoribbon, we confirm the single-crystal, rhombohedral structure of the ribbons.

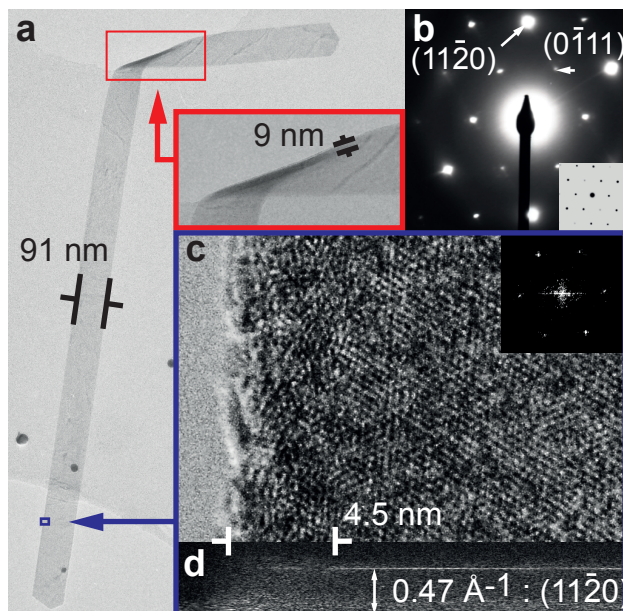


Figure 2: (a) TEM image of a $2 \mu\text{m}$ long nanoribbon folding around the pore of a TEM grid. Growth conditions for this sample were: $T_g = 480 \text{ }^\circ\text{C}$, $P = 100 \text{ Torr}$, $t = 30 \text{ min}$, 600 sccm flow of H_2 , $p_{\text{TMBi}} = 1 \times 10^{-5} \text{ atm}$, $r = 30$. A fold in the nanoribbon reveals a thickness of 9 nm . (b) TEM electron diffraction pattern. The inset shows the expected diffraction pattern. (c) A HRTEM image shows that the nanoribbon is single crystal (inset: Fourier transform obtained from the real space image). (d) The FFT of the columns of the image in (c) shows a peak at 0.47 \AA^{-1} , consistent with the $(11\bar{2}0)$ growth direction. The peak fades at the edge of the nanoribbon, indicating an amorphous region with width $\sim 4.5 \text{ nm}$, typical of atmospherically exposed samples.

The nanoribbons grow in the $(11\bar{2}0)$ direction with lattice constant $a = 4.1 \text{ \AA}$, consistent with the spacing expected from the bulk crystal structure. TEM-based energy dispersive X-ray spectroscopy (EDS) indicates a 2:3 ratio of Bi and Se in the nanoribbons to within the accuracy of the measurement. The samples are exposed to atmosphere after growth and exhibit an amorphous edge region several nanometers wide. The upper and lower surfaces, which lack the dangling bonds as on the edges, must have considerably less irregularity, or crystallinity would not be observed in samples as thin as in Figure 2.

A large fraction of the crystallites shown in Figure 1a are partially transparent under the SEM (at 30 keV), indicating the formation of very thin, suspended nanoplates. We use TEM and AFM to quantitatively extract the sample thickness. By directly imaging the thicknesses of wires bent around the pores of the TEM grids (as in Figure 2) we find an average thickness of $\sim 10 \text{ nm}$. An AFM study of 18 nanoribbons gives thicknesses $20 \pm 10 \text{ nm}$. The discrepancy is probably due to an unintentional thickness bias imposed during sample preparation for the two imaging methods. The nanoribbon thicknesses lie below the distribution of dimensions produced in the solid-source method referred to above. We find that the solid-source growth method typically produces ribbons 30–100 nm in thickness, consistent with other reports in the literature.¹⁹

Ribbons are further characterized by low-temperature magnetotransport measurements, which are summarized in Figure 3. Four probe devices are made by eliminating the native oxide in e-beam defined contact areas using a low-energy ion etch, followed by thermal evaporation of Ti/Au contacts. We have studied a nanoribbon with thickness $17 \pm 5 \text{ nm}$, width $W = 170 \pm 5 \text{ nm}$, and length $L = 380 \pm 10 \text{ nm}$, where dimensions were measured by SEM after performing transport measurements. Using these dimensions, the calculated resistivity is $4 \pm 1 \text{ m}\Omega\text{-cm}$, similar to that of bulk and nanoribbon Bi_2Se_3 samples with $n = 10^{18} \text{ cm}^{-3}$. The resistance versus temperature profile is also similar to such samples, having a metallic profile at high temperatures and a $\log(T)$ dependence below 10 K.^{6,7,13} The temperature dependence is consistent with weak anti-localization (WAL) in Bi_2Se_3 , which we further explore by measuring the magnetoconductance.

Perpendicular magnetic field sweeps at 4.2 K, 0.50 K, and 0.29 K show reproducible, aperiodic

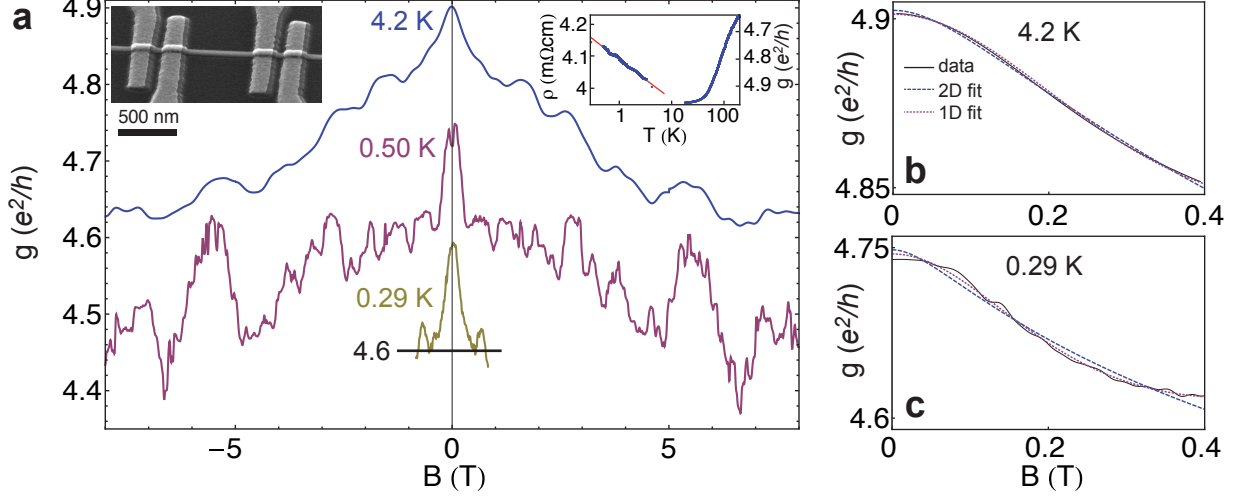


Figure 3: (a) The four probe conductance of a nanoribbon in perpendicular magnetic field shows weak anti-localization and universal conductance fluctuations. The trace taken at 0.29 K is offset for clarity. Left inset: SEM image of a typical device. Right inset: Sample resistivity as a function of temperature shows a metallic dependence above 10 K, typical of Bi_2Se_3 samples. (b–c) Low field data taken at 4.2 K and 0.29 K are fit to 2D (ribbon width greater than the coherence length) and 1D (ribbon width less than the coherence length) models of weak anti-localization.

fluctuations consistent with universal conductance fluctuations, and a low field conductance peak consistent with WAL in Bi_2Se_3 .⁸ The presence of conductance fluctuations indicates that the coherence length is on the same order as the sample dimensions. We fit the low field data ($|B| < 0.4$ T) at 4.2 K and 0.29 K to the 2D WAL model, which is valid in the limit of $W \gg l_\phi \gg l_{so}$,

$$\Delta g = \alpha \frac{e^2}{\pi h} \left[\ln \left(\frac{B_\phi}{B} \right) - \Psi \left(\frac{1}{2} + \frac{B_\phi}{2B} \right) \right] \quad (1)$$

where $\Delta g = g(B) - g(B = 0)$, Ψ is the digamma function, h is Planck's constant, e is the elementary charge, $\alpha=1/2$ for a single 2D channel, and the phase breaking field $B_\phi = h/4el_\phi^2$ is defined in terms of the coherence length l_ϕ .²⁸ We take α and l_ϕ as fit parameters. At 4.2 K and 0.29 K, we obtain $\alpha = 0.41$ and 0.43 respectively, consistent with a single coherent conduction channel.⁹ At 4.2 K we find $l_\phi = 119$ nm, but at 0.29 K we find $l_\phi = 192$ nm which is greater than the channel width, invalidating the 2D treatment at that temperature. We therefore also fit according to a diffusive 1D model, which is valid for $l_\phi \gg W$,^{29,30}

$$\Delta g = -\frac{2e^2}{hL} \left[\frac{3}{2} \left(\frac{1}{l_\phi^2} + \frac{4}{3} \frac{1}{l_{so}^2} + \frac{1}{3} \left(\frac{eWB}{h} \right)^2 \right)^{-\frac{1}{2}} - \frac{1}{2} \left(\frac{1}{l_\phi^2} + \frac{1}{3} \left(\frac{eWB}{h} \right)^2 \right)^{-\frac{1}{2}} \right]. \quad (2)$$

Taking l_{so} and l_ϕ as fit parameters, Eqn. (2) provides a marginally better fit to the WAL peak at 4.2 K (yielding $l_\phi = 113$ nm and $l_{so} = 69$ nm) and a visibly better fit at 0.29 K, where we obtain $l_\phi = 178$ nm and $l_{so} = 93$ nm. The consistency of the two treatments suggests that the coherence length crosses over between the 2D and 1D limits in this temperature range. The observed short spin-orbit length likely arises from a combination of transport through the surface states and bulk states that are spin-split by surface Rashba fields, and is comparable in magnitude to other strong spin-orbit nanomaterials such as InAs nanowires.^{31,32}

In summary, we demonstrate the synthesis of Bi_2Se_3 nanostructures using MOCVD. MOCVD allows independent control of the Bi and Se concentration during growth. High resolution electron microscopy confirms that the samples exhibit a high degree of structural order. Magneto-transport measurements yield a spin-orbit length $l_{so} \sim 100$ nm, and phase coherence length $l_\phi = 100\text{--}200$ nm. Four-probe measurements give a resistivity of 4 m Ω -cm, indicating that the doping levels are comparable to Bi_2Se_3 samples grown using other methods. The measured phase coherence lengths are also similar to samples fabricated by other means.^{8,27} Our results indicate that MOCVD samples are of sufficiently high quality to enable transport based studies. Further work is required to clarify and refine the growth mechanism, and to determine whether similar MOCVD processes are possible in more sophisticated TI materials such as $\text{Bi}_2\text{Te}_2\text{Se}$.³³

Acknowledgement

We thank Bob Cava and Phuan Ong for useful discussions, Sian Dutton, Minkyung Jung, Sunanda Koduvayur Parthasarathy, Chris Quintana, and Jian Zhang for technical contributions, and Nan Yao at the Princeton Imaging and Analysis Center for assistance characterizing samples. Research was supported by the Sloan and Packard Foundations, and the NSF funded Princeton Center for Complex Materials, DMR-0819860. We acknowledge the use of the PRISM Imaging and Analysis

Center, which is supported in part by the NSF MRSEC program.

References

- (1) Hasan, M.; Kane, C. *Rev. Mod. Phys.* **2010**, *82*, 3045–3067.
- (2) Qi, X.-L.; Zhang, S.-C. *Rev. Mod. Phys.* **2011**, *83*, 1057–1110.
- (3) Xia, Y.; Qian, D.; Hsieh, D.; Wray, L.; Pal, A.; Lin, H.; Bansil, A.; Grauer, D.; Hor, Y. S.; Cava, R. J.; Hasan, M. Z. *Nature Phys.* **2009**, *5*, 398–402.
- (4) Roushan, P.; Seo, J.; Parker, C.; Hor, Y. S.; Hsieh, D.; Qian, D.; Richardella, A.; Hasan, M. Z.; Cava, R. J.; Yazdani, A. *Nature* **2009**, *460*, 1106–1109.
- (5) Hor, Y. S.; Richardella, A.; Roushan, P.; Xia, Y.; Checkelsky, J. G.; Qian, D.; Richardella, A.; Yazdani, A.; Hasan, M. Z.; Ong, N. P.; Cava, R. J. *Phys. Rev. B* **2009**, *79*, 195208.
- (6) Analytis, J. G.; Ross, D. M.; Riggs, S. C.; Chu, J.-H.; Boebinger, G. S.; Fisher, I. R. *Nature Phys.* **2010**, *6*, 960–964.
- (7) Checkelsky, J. G.; Hor, Y. S.; Liu, M.-H.; Qu, D.-X.; Cava, R. J.; Ong, N. P. *Phys. Rev. Lett.* **2009**, *103*, 246601.
- (8) Checkelsky, J. G.; Hor, Y. S.; Cava, R. J.; Ong, N. P. *Phys. Rev. Lett.* **2011**, *106*, 196801.
- (9) Steinberg, H.; Laloë, J.-B.; Fatemi, V.; Moodera, J. S.; Jarillo-Herrero, P. *Phys. Rev. B* **2011**, *84*, 233101.
- (10) Kim, C.; Cho, S.; Butch, N. P.; Syers, P.; Kirshenbaum, K.; Shaffique, A.; Paglione, J.; Fuhrer, M. S.; *Nature Phys.* **2012**, *8*, 460.
- (11) Peng, H.; Lai, K.; Kong, D.; Meister, S.; Qi, X.-L.; Zhang, S. C.; Cui, Y. *Nature Mater.* **2010**, *9*, 225–229.

- (12) Xiu, F.; He, L.; Wang, Y.; Cheng, L.; Chang, L.-T.; Lang, M.; Huang, G.; Kou, X.; Zhou, Y.; Jiang, X.; Chen, Z.; Zou, J.; Shailos, A.; Wang, K. L. *Nature Nanotech.* **2011**, *6*, 216–221.
- (13) Hong, S. S.; Cha, J. J.; Kong, D.; Cui, Y. C. *Nature Comm.* **2012**, *3*, 757.
- (14) Pérez Vicente, C.; Tirado, J. L.; Adouby, K.; Jumas, J. C.; Abba Touré, A.; Kra, G. *Inorg. Chem.* **1999**, *38*, 2131–2135.
- (15) Dresselhaus, M. S.; Chen, G.; Tang, M. Y.; Yang, R. G.; Lee, H.; Wang, D. Z.; Ren, Z. F.; Fleurial, J.-P.; Gogna, P. *Adv. Mater.* **2007**, *19*, 1043–1053.
- (16) Cui, H. M.; Liu, H.; Li, X.; Wang, J. Y.; Han, F.; Zhang, X. D.; Boughton, R. I. *J. Solid State Chem.* **2004**, *177*, 4001–4006.
- (17) Jagminas, A.; Valsiunas, I.; Veronese, G.; Juskenas, R.; Rutavicius, A. *J. Cryst. Growth* **2008**, *310*, 428–433.
- (18) Lee, J. S.; Brittman, S.; Yu, D.; Park, H. *J. Am. Chem. Soc.* **2008**, *130*, 6252–6258.
- (19) Kong, D.; Randel, J. C.; Peng, H.; Cha, J. J.; Meister, S.; Lai, K.; Chen, Y.; Shen, Z.-X.; Manoharan, H. C.; Cui, Y. *Nano Lett.* **2010**, *10*, 329–333.
- (20) Al Bayaz, A.; Giani, A.; Artaud, M. C.; Foucaran, A.; Pascal-Delannoy, F.; Boyer, A. *J. Cryst. Growth* **2002**, *241*, 463–470.
- (21) Lin, Y.-F.; Chang, H.-W.; Lu, S.-Y.; Liu, C. W. *J. Phys. Chem. C* **2007**, *111*, 18538–18544.
- (22) Schroer, M. D.; Xu, S. Y.; Bergman, A. M.; Petta, J. R. *Rev. Sci. Instrum.* **2010**, *81*, 023903.
- (23) Schroer, M. D.; Petta, J. R. *Nano Lett.* **2010**, *10*, 1618–1622.
- (24) Precursors are available from Strem Chemicals Inc. and SAFC Hitech.
- (25) Kolasinski, K. *Curr. Opin. Solid State Mater. Sci.* **2006**, *10*, 182–191.
- (26) Mohammad, S. N. *J. Appl. Phys.* **2010**, *107*, 114304.

- (27) Cha, J. J.; Kong, D.; Hong, S.-S.; Analytis, J. G.; Lai, K.; Cui, Y. *Nano. Lett.* **2012**, *12*, 1107–1111.
- (28) Hikami, S.; Larkin, A. I.; Nagaoka, Y. *Prog. Theor. Phys.* **1980**, *63*, 707–710.
- (29) Santhanam, P.; Wind, S.; Prober, D. E. *Phys. Rev. Lett.* **1984**, *53*, 1179–1182.
- (30) Roulleau, P.; Choi, T.; Riedi, S.; Heinzl, T.; Shorubalko, I.; Ihn, T.; Ensslin, K. *Phys. Rev. B* **2010**, *81*, 155449.
- (31) King, P. D. C.; Hatch, R. C.; Bianchi, M.; Ovsyannikov, R.; Lupulescu, C.; Landolt, G.; Slomski, B.; Dil, J. H.; Guan, D.; Mi, J. L.; Rienks, E. D. L.; Fink, J.; Lindblad, A.; Svensson, S.; Bao, S.; Balakrishnan, G.; Iversen, B. B.; Osterwalder, J.; Baumberger, F.; Hofmann, P. *Phys. Rev. Lett.* **2011**, *107*, 096802.
- (32) Hansen, A. E.; Björk, M. T.; Fath, C.; Thelander, C.; Samuelson, L. *Phys. Rev. B* **2005**, *71*, 205328.
- (33) Ren, Z.; Taskin, A. A.; Sasaki, S.; Segawa, K.; Ando, Y. *Phys. Rev. B* **2010**, *82*, 241306.